ORIGINAL PAPER

A novel ternary Y-DNA walker amplification strategy designed fluorescence aptasensor based on Au@SiO$_2$@Fe$_3$O$_4$ nanomaterials for ochratoxin A detection

Xiaoze Dong[1] · Shuo Qi[1] · Mingwei Qin[1] · Ning Ding[1] · Yin Zhang[2] · Zhouping Wang[1,2,3]

Abstract

A novel ternary Y-DNA walker amplification strategy designed fluorescence aptasensor based on Au@SiO$_2$@Fe$_3$O$_4$ nanomaterials for ultrasensitive and specific ochratoxin A detection in food samples is presented. Au@SiO$_2$@Fe$_3$O$_4$ nanomaterials provide the loading platform as well as separation and recovery properties for the ternary Y-DNA walker. The ternary Y-DNA walker is designed to be driven by Nb.BbvCI cleaving a large number of FAM probes to achieve signal amplification. Since Ochratoxin A (OTA) can bind to the constituent aptamer in the ternary Y-DNA walker, adding OTA will destroy the structure of the ternary Y-DNA walker, thereby inhibiting the driving process of the walker. After optimization of various parameters, a standard curve was obtained from 100 to 0.05 ng·mL^{-1} of OTA with the limit of determination of 0.027 ng·mL^{-1}. The spiked recovery of peanut samples by this method was 82.00–93.30%, and the aptasensor showed excellent specificity and long-term stability. This simple, robust, and scalable oligonucleotide chain-based ternary Y-DNA walker can provide a general signal amplification strategy for trace analysis.

Keywords OTA · Aptamer · DNA walker · Aptasensor · Magnetic nanomaterials

Introduction

Ochratoxin A (OTA) is a secondary metabolite secreted of several *Aspergillus* and *Penicillium* spp [1]. First time from a commercial corn sample in 1969 [2], OTA is the most prevalent and toxic member of the ochratoxin group, exhibiting neurotoxicity, immunotoxicity, teratogenicity, and mutagenicity due to its chemical structure (i.e., chlorine atoms in molecular substituents) and is classified as a Group 2B carcinogen to humans [3, 4]. In 2020, the report of the EFSA Panel on Contaminants in the Food Chain (CONTAM), a Benchmark dose limit (BMDL$_{10}$) of 4.73 µg·kg^{-1} body weight (bw) per day was calculated from kidney lesions observed in pigs [5]. In fact, OTA is capable of contaminating most food products (including cereals, coffee, and wine) and is the only mycotoxin with established regulatory limits in wine [6]. With the global prevalence of OTA estimated at 53% according to risk assessment studies [7], it is extremely important and urgent to develop specific and sensitive strategies for the detection of OTA in food.

Current proven and widely used detection methods such as mass spectrometry (molecular analysis for chemical detection) and running qPCR (for DNA amplification). These methods require expensive instrumentation, operating costs, trained technicians, and sample shipping costs for centralized analysis [8, 9]. Fluorescence-based sensing technologies offer unparalleled sensitivity and richness in addition to low cost, which allows for unique studies of small molecules or structured biomacromolecules [10, 11]. Aptamer is a class of short single-stranded DNA (ssDNA) or RNA oligonucleotides [12, 13]. Aptamers are suitable recognition elements, due to their small size, high stability, high affinity, and strong specificity [14, 15]. Aptamer can not

✉ Zhouping Wang
  wangzp@jiangnan.edu.cn

1 State Key Laboratory of Food Science and Technology, International Joint Laboratory On Food Safety, Jiangnan University, Wuxi 214122, China

2 Key Laboratory of Meat Processing of Sichuan, Chengdu University, Chengdu 610106, China

3 School of Food Science and Technology, National Engineering Research Center for Functional Food, Collaborative Innovation Center of Food Safety and Quality Control in Jiangsu Province, Food, Jiangnan University, Wuxi 214122, China

only be isolated and combined with any selected molecule (including metal ions, small molecules, peptides, proteins, and even material surfaces), but also can be easily modified [16, 17]. Aptamer-based fluorescent biosensors have received extensive attention due to their high sensitivity, specificity, fast response, and relatively low cost [18, 19].

Using a "bottom-up" approach, it has been possible to construct complex DNA nanostructures with high biosensing potential. It involves the self-folding of single-oligonucleotide DNA and multiple-oligonucleotides complementary pairing, and can form two-dimensional or three-dimensional structures, such as sheets or more complex structures with edges and planes [20, 21]. These DNA nanostructures can be programmed with aptamers and oligonucleotides to respond to external stimuli, such as biomolecules, enabling their use in biosensing strategies [22]. The DNA walker is one of the dynamic DNA nanostructures, which has good controllability and excellent predictability [23, 24]. Due to they can move autonomously along programmed oligonucleotide trajectories to elicit hundreds of signaling molecules with high specificity in response to a single binding event, they offer interesting strategies for designing signal amplification methods. Aptamer (Apt)-conjugated nanomaterials have been used by researchers as part of a solution for building biosensors to monitor food hazards [25]. The characteristics of separation and recovery can be provided for fluorescent sensors by coupling aptamers to Fe_3O_4 nanomaterials [26]. Fe_3O_4 nanomaterials do have their limitations, such as fast agglomeration and high surface energy, resulting in the magnetic loss [27]. Modification by conjugating a SiO_2 coating to the surface of Fe_3O_4 nanomaterials avoids oxidation and agglomeration [28]. Moreover, the SiO_2 coating can also provide chemical and physical shielding from the external environment, which prevents flocs of particles and substances from adsorbing to the surface, thus improving chemical and optical stability [29].

In this work, we attempted to develop a fluorescent aptasensor designed based on a novel DNA walker strategy, and the introduction of magnetic nanocomposites endowed the sensor with certain easy-to-detect properties. We synthesized iron oxide and silica core–shell loaded gold nanoparticles composites ($Au@SiO_2@Fe_3O_4$) nanomaterials as a sensing platform endowed with recovery and separation properties. SiO_2 coating can avoid Fe_3O_4 nanomaterials oxidation and agglomeration and improve its chemical and optical stability. The ternary Y-DNA walker is covalently bound to the surface of the $Au@SiO_2@Fe_3O_4$ via Au–S affinity. The restriction endonuclease Nb.BbvCI can drive the DNA walker to cleave the FAM probes, which releases the FAM probes in the supernatant by magnetic separation. Due to the ability of OTA to disrupt the Y-shaped DNA walker, OTA concentration is inversely proportional to the concentration of FAM probes released by cleavage. Based

on the high specificity and amplification characteristics of the DNA walker, as well as the separation performance and recovery characteristics of magnetic nanomaterials, it exhibits superior performance in the detection of OTA with ultrasensitivity, specificity, and stability.

Experimental section

Materials, reagents, and apparatus

Oligonucleotides were synthesized and purified with HPLC by Sangon Biotechnology Co., Ltd. (Shanghai, China). The OTA aptamer 1.12.8 (Apt), screened by Penner's research group in 2001 [30], was used as the recognition element in this work. Table S1 shows detailed sequence information of all oligonucleotides.

Ochratoxin A (OTA), zearalenone (ZEN), Deoxynivalenol (DON), Aflatoxin B_1 (AFB_1), and Fumonisin B_1(FB_1) were obtained from Sigma-Aldrich. Nb.BbvCI (10,000 units·mL^{-1}) and 10×CutSmart Buffer (50 mM potassium acetate, 20 mM Tris-base, 10 mM Mg^{2+}, 100 µg·mL^{-1} BSA) were obtained from New England Bio-labs (America). Iron trichloride hexahydrate ($FeCl_3$·$6H_2O$, 99%), Poly (acrylic acid) (PAA, average M_w 1800), Tris(hydroxymethyl) aminomethane (Tris-base), Gold chloride trihydrate ($HAuCl_4$·$3H_2O$, ≥ 99.9%), Tetraethyl orthosilicate (TEOS, 99.99% metals basis), Tris(hydroxymethyl) aminomethane phosphine hydrochloride solution (TCEP, 98%), polyethylenimine (PEI, BR, 99%, molecular weight 10000, liquid) sodium chloride (NaCl), magnesium chloride ($MgCl_2$), potassium chloride (KCl), and concentrated ammonia solution (NH_3·H_2O, 28 wt%) were obtained from Yuanye Bio-Technology Co., Ltd. (Shanghai, China). Ultrapure water was used throughout the experiments and all chemicals were of analytical grade.

Reagents: 10×BB buffer (50 mM Tris-base, 5 mM K^+, 100 mM Na^+, 1 mM Mg^{2+}, pH 7.4), 10×Tris–HCl buffer (20 mM Tris-base, 5 mM K^+, 50 mM Na^+, pH 7.4). The 20 mM FAM-cDNA stock solution and the 20 mM H-DNA were configured with 10 mM TCEP, Tris–HCl buffer. Other oligonucleotides stock solution was configured with Tris–HCl buffer.

Apparatus: Materials were characterized by transmission electron microscope (TEM, JEM-2100HR, JEOL Ltd., Japan), scanning electron microscopy (SEM, 3 kV, Hitachi Ltd., Japan), X-ray diffractometer (XRD, Cu-Kα, λ = 0.15406 nm, D2 PHASER, Bruker AXS Co., Ltd., German). The oligonucleotide chains were incubated in Bio-Rad C1000 Thermal Cycler (Bio-Rad Co USA) and Flexi-Therm constant temperature incubator (Vitl, UK). PowerPac Basic Power Supply and Molecular Imager® Gel Doc™ XR + System with Image Lab™ Software (BioRad

Co., US) were used for gel electrophoresis and imaging, respectively. Fluorescence signals were collected Synergy H1 multi-detection microplate reader (BioTek Instruments, Inc., US).

The detailed procedures for synthesis of Au@SiO$_2$@Fe$_3$O$_4$ nanomaterials were given in the Supporting Information (Sect. 1).

Preparation of fluorescence aptasensor

Yn-DNA was constructed by the annealing of three single-stranded DNAs [Apt, H-DNA, and En-DNA hybridization ($n = 5, 20, 40$, represents the number of consecutive T bases in the oligonucleotides)]. Generally, the three oligonucleotides [Apt, H-DNA, En-DNA ($n = 5, 20, 40$)] stock solutions were separately dissolved in Tris–HCl buffer. Afterward, they were blended with equal volumes to a final concentration of 1 mM. The mixture was heated to 95 °C for 5 min and then cooled for 3 h to room temperature. The FAM-DNA was individually dissolved in Tris–HCl buffer to a final concentration of 1 mM.

The Au@SiO$_2$@Fe$_3$O$_4$ nanomaterials were resuspended in ultrapure water to prepare a 2-mg·mL^{-1} standard solution. Au@SiO$_2$@Fe$_3$O$_4$ nanomaterials will gradually sediment, so vortex measurements often. Add a certain volume ratio of Yn-DNA and FAM-DNA to the Au@SiO$_2$@Fe$_3$O$_4$ nanomaterials dispersion solution, 200r shake, and incubate for 2 h at 37 °C to prepare fluorescence aptasensor based on ternary Y-DNA walker amplification strategy.

Detection of fluorescence aptasensor

Before measurement, a mixture solution consisting of Nb.BbvCI, NEB buffer, and specific concentrations of OTA was dropped on the aptasensor and 200r shake and incubated for 3 h at 37 °C. The supernatant was collected by magnetic separation for fluorescence detection. For each example detection setup, all experiments were prepared in triplicate at the 200 μL scale. Each experiment consisted of 20–60 μL 2 mg·mL^{-1} of Au@SiO$_2$@Fe$_3$O$_4$ standard solution, 20 μL of 10 × BB buffer, 2 μL 10000 units·mL^{-1} Nb.BbvCI, 20 μL 10 × CutSmart Buffer, 10 μL 1 mM Yn-DNA, 20–60 μL 1 mM FAM-DNA, and 10 μL of specific concentrations of OTA. Finally, take 120 μL of supernatant was by magnetic separation and transferred into a 96-well plate. The FAM fluorescence signal was recorded from 508 to 650 nm with excitation at 480 nm at room temperature by Synergy H1 multi-detection microplate reader. For the measured analytical signal, excitation of FAM fluorescence was performed at 480 nm and emission of FAM was recorded at 522 nm.

Detection of OTA in spiked peanut samples

10 mL extraction solution (CH$_3$OH: H$_2$O = 7:3, v:v) was placed in a 50-mL centrifuge tube, and 25 mL crushed peanut dispersion solution (containing 2 g crushed peanut) was added to the extraction solution. After shaking incubation for 15 min, the sample solution was centrifuged at 5000 r/min for 10 min. The top aqueous layer was decanted into a round flask, and the aqueous layer was tenfold diluted with the Tris–HCl solution. For the standard addition and recovery experiments, the OTA standard solutions were added to the ground maize samples before adding the extracting solution.

Results and discussion

Assay strategy

We developed a fluorescence aptasensor based on a ternary Y-DNA walker amplification strategy for OTA detection analysis in food samples. The detailed working principle is shown in Scheme 1. To achieve the pretreatment of ternary Y-DNA walker sensors and the enrichment of fluorescent signals, Au@SiO$_2$@Fe$_3$O$_4$ nanomaterials were synthesized and used. Scheme 1 A shows the synthesis procedure of Au@SiO$_2$@Fe$_3$O$_4$. Generally, Yn-DNA (Constituents H-DNA) and FAM-cDNA are immobilized on the surface of Au@SiO$_2$@Fe$_3$O$_4$ via Au–S self-assembly. The high specific surface area of the Au@SiO$_2$@Fe$_3$O$_4$ provides a high density of oligonucleotide sites, and then enough Yn-DNA and FAM-cDNA are installed. Scheme 1 B shows the preparation of the ternary Y-DNA walker sensor. Inset I shows a close-up of the tertiary structure of the OTA aptamer bound to its ligand, based on the PDB structure 6J2W [31]. Inset II shows the detailed base-binding sequence of the Yn-DNA. The 3' end of the Yn-DNA (Constituent En-DNA) can be complementary to the base of the hairpin region of FAM-cDNA to form a restriction endonuclease Nb.BbvCI specific recognition sequence (5'…CCTCAGC…3', 3'…GGAGT^CG…5'). Nb.BbvCI only cuts the FAM-cDNA hairpin region (containing the base sequence GGAGTCG), causing the 3' end of Yn-DNA (Constituent En-DNA) to be released from the construct to initiate the next hybridization process. The abundant cleaved FAM probes were generated during cycling. In the presence of OTA, OTA dissociates the aptamer from Yn-DNA (Constituent Apt), thereby disrupting the Yn-DNA structure. Constituents En-DNA and H-DNA cannot form a Yn-DNA, so the dissociation of the aptamer will lead to the destruction of the ternary Y-DNA walker, so FAM-cDNA cannot be effectively cut. Scheme 1 C shows the sensor differences in the presence and absence of OTA, the fluorescence intensity of FAM is inversely proportional to the OTA concentration.
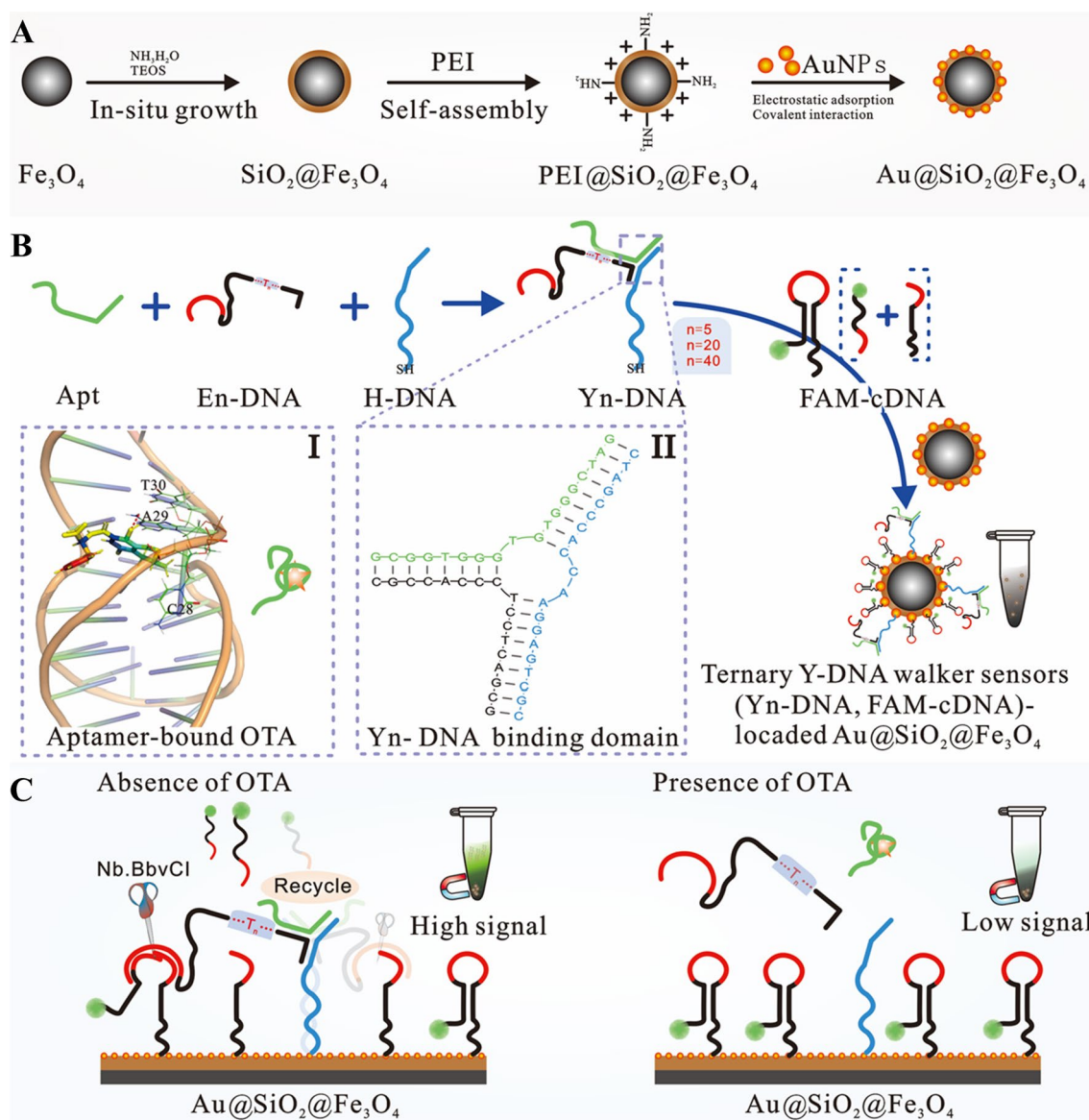
Scheme 1 **A** Schematic diagram of Au@SiO$_2$@Fe$_3$O$_4$ synthesis procedures; **B** Engineering strategy of ternary Y-DNA walker sensors; Inset I shows a close-up of the tertiary structure of the OTA aptamer bound to its ligand, based on the PDB structure 6J2W [31]. Inset II shows the detailed base-binding sequence of the Yn-DNA. **C** Detection procedure for ternary Y-DNA walker sensors machines in presence and absence of OTA

Characterization of materials

The surface morphology of SiO$_2$@Fe$_3$O$_4$ and Au@SiO$_2$@Fe$_3$O$_4$ was characterized by scanning electron microscopy (SEM). Comparing Fig. 1A and B, it can be observed that gold nanoparticles (AuNPs) are successfully modified on the surface of SiO$_2$@Fe$_3$O$_4$. The Fig. S1 further shows the SEM image of the Au@SiO$_2$@Fe$_3$O$_4$ with 300 nm scale, during which the broken of Au@SiO$_2$@Fe$_3$O$_4$ (Fig. 1C) was found accidentally, further confirming that the Au@SiO$_2$@Fe$_3$O$_4$ has a core–shell structure. The particle sizes of Fe$_3$O$_4$, SiO$_2$@Fe$_3$O$_4$, and Au@SiO$_2$@Fe$_3$O$_4$, respectively,

were characterized by transmission electron microscopy (TEM). As shown in Fig. 1 D, the average diameter of the obtained Fe$_3$O$_4$ microspheres is about 436 nm, and the surface is rough. After coating with SiO$_2$, the microspheres exhibited an obvious core–shell structure, and the thickness of the SiO$_2$ shell was about 124 nm (Fig. 1E). The diameter of the subsequently loaded AuNPs is about 25 nm (Fig. 1F). The Fig. S2 shows the TEM images of Au@SiO$_2$@Fe$_3$O$_4$ (Fig. S2A) with 200 nm scale, and magnetic characterization images (Fig. S2B) of 0.5 mg·mL^{-1} Au@SiO$_2$@Fe$_3$O$_4$ aqueous dispersion solution. These results demonstrate the successful synthesis of Au@SiO$_2$@Fe$_3$O$_4$ nanomaterials
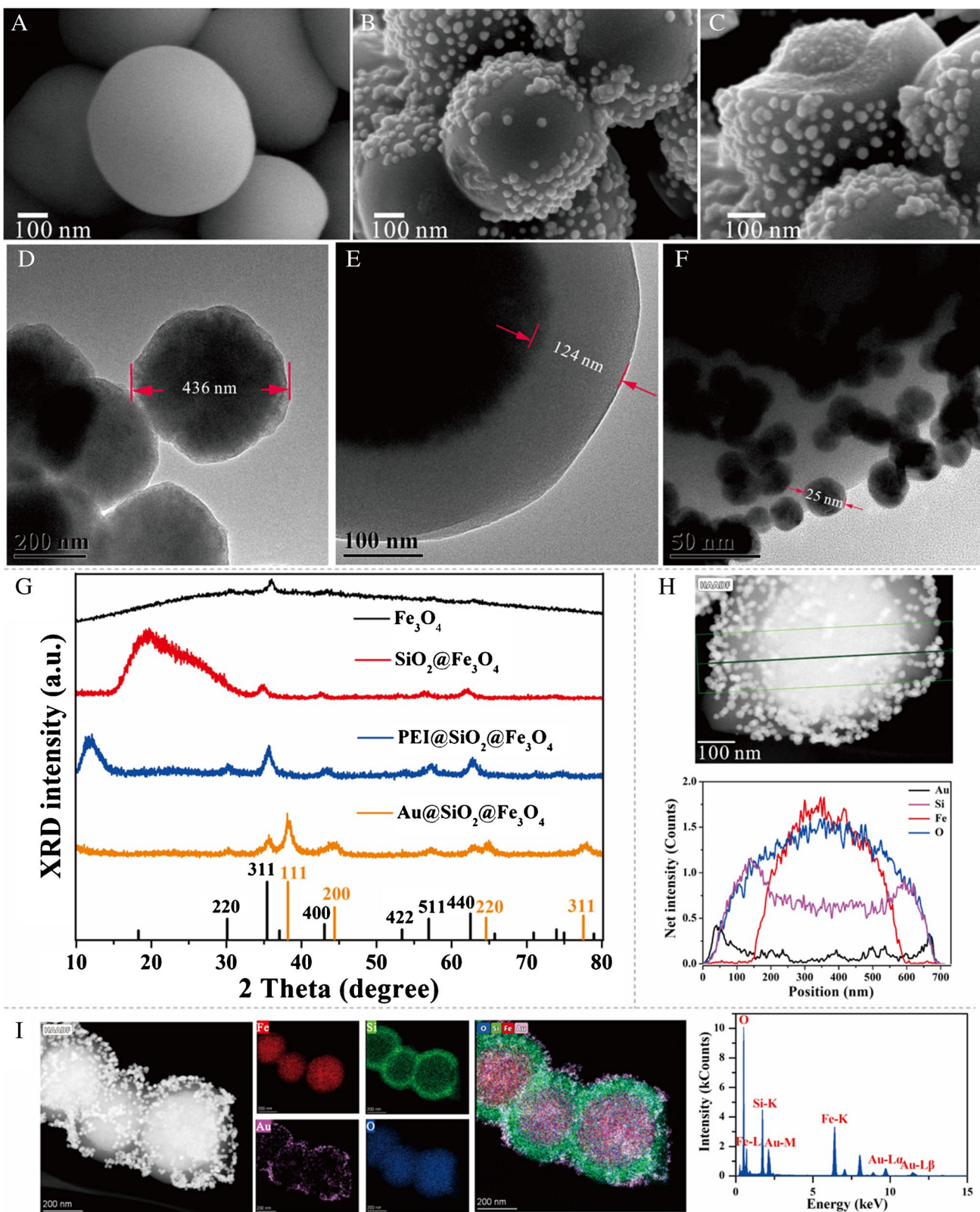
Fig. 1 SEM image of $SiO_2@Fe_3O_4$ (**A**), $Au@SiO_2@Fe_3O_4$ (**B**), and broken of $Au@SiO_2@Fe_3O_4$ (**C**); TEM image of Fe_3O_4 (**D**), $SiO_2@Fe_3O_4$ (**E**), and $Au@SiO_2@Fe_3O_4$ (**F**); XRD patterns of synthesis process and crystal structure changes of $Au@SiO_2@Fe_3O_4$ (**G**); Line scan (**H**) and elemental mapping images (**I**) of Fe, Si, Au, and O in $Au@SiO_2@Fe_3O_4$

with separation and recovery properties, which can be used as immobilized platforms for ternary Y-DNA walker. Au@Fe3O4 nanomaterials was used as the control group, and its TEM images with 200 nm scale is shown in Fig. S3.

The synthesis process and crystal structure changes of Au@SiO_2@Fe_3O_4 nanomaterials were further investigated by X-ray diffraction (XRD). As shown in Fig. 1 G, Fe_3O_4 nanomaterials exhibit "Fe_3O_4" characteristic reflective surfaces of (220), (311), (400), (422), (511), and (440) at 2θ values of 30.6°, 35.9°, 43.2°, 54.2°, 57.4°, and 62.9°, respectively, with space group: Fd-3 m[227], equiaxed crystal system [JCPDS Card. No. PDF#26–1136]. SiO_2@Fe_3O_4 nanoparticles at 2θ values of around 20° exhibit a dome-shaped scattering curve, which is a typical diffraction peak of amorphous SiO_2 (JCPDS Card. No. PDF#27–0605, not shown in the figure), that is, the irregular structure composed of silicon-oxygen tetrahedra network. PEI@SiO_2@Fe_3O_4 nanoparticles showed an improved degree of crystallization, which may be due to the destruction of the mesoporous structure of SiO_2 after PEI coating. Moreover, the strong peak at 2θ values of 12° also corresponds to the d-space value of 6.82 Å, which can indicate the characteristic peak of PEI polymer [32, 33]. Au@SiO_2@Fe_3O_4 nanoparticles exhibit "Au" characteristic reflective surfaces of (111), (200), (220), and (311) from 2θ values of 38.6°, 44.8°, 65.0°, and 78.0°, respectively, with space group: Fd-3 m [225], equiaxed crystal system [JCPDS Card. No. PDF#04–0784], confirmed that the AuNPs were successfully decorated to the surface of SiO_2@Fe_3O_4 nanoparticles. Analysis of line scan and elemental mapping images profiles reveals that Fe, Si, Au, and O elements have distinct layered core–shell structures. The line scan images are shown in Fig. 1 H, the arrangement of elements from the outer shell to the inner core is Au (pink), Si (green), and Fe (red) elements, and the O (indigo) element is highly overlapped with Si and Fe elements. The elemental mapping images is shown in Fig. 1I, which has a more intuitive display of the element distribution and composition of Au@SiO_2@Fe_3O_4.

Characterization of ternary Y-DNA walker sensor

The key to the ternary Y-DNA walker sensor is the successful construction of Yn-DNA, so it is necessary to verify the formation of the Yn-DNA first. Yn-DNA involves three constituents: Apt, H-DNA, and En-DNA. Native polyacrylamide gel electrophoresis (PAGE) was used to characterize and validate the formation of Yn-DNA. Use Image Lab™ software to compare the separated bands of different oligonucleotide chain constituents at known concentrations (0.4 μM). The electrophoresis analysis was performed in 1 × TBE buffer at 4℃ for 50 min with 15% Polyacrylamide gels (30%, acrylamide/bis-acrylamide 29:1). As shown in Fig. 2A, lanes 1, 2 and 3 correspond to Apt, H-DNA, and E20-DNA,

respectively. Lanes 4, 5, and 6 correspond to constituents Apt, H-DNA, constituents Apt, E20-DNA, and constituents H-DNA, E20-DNA, respectively. Although new bands appeared in lines 4 and 5, the bands were still very weak, indicating that constituents Apt, H-DNA, and constituents Apt, E20-DNA were only weakly bound. Moreover, Line 5 did not appear any new bands, indicating that constituents Apt and E20-DNA did not bind. Lane 7 corresponds to constituents Apt, H-DNA, E20-DNA, and a bright band appears, which proves the successful synthesis of Y20-DNA. Lanes 8 and 9 correspond to constituents Apt, H-DNA, and E5-DNA and constituents Apt, H-DNA, and E40-DNA, respectively, which further proves the successful synthesis of Y5-DNA and Y40-DNA, and also proves that the continuous T base sequence does not affect the synthesis of Yn-DNA.

Moreover, using UV–vis absorption spectroscopy provided direct evidence about the successful loading of the Y ternary Y-DNA walker on the surface of Au@SiO_2@Fe_3O_4 nanomaterials via Au–S affinity. As shown in Fig. 2B, the ternary Y-DNA walker (Constituents Apt, H-DNA, E20-DNA, and FAM-cDNA) has a characteristic peak at 260 nm. After the ternary Y-DNA walker was incubated with the magnetic Au@SiO_2@Fe_3O_4 nanomaterial, the decrease of the characteristic peaks of the supernatant obtained by magnetic separation confirmed the successful coupling of the ternary Y-DNA walker with Au@SiO_2@Fe_3O_4.

Each key step of the ternary Y-DNA walker sensor was further characterized by detecting the fluorescent signal of FAM. As shown in Fig. 2C, the ternary Y-DNA walker (indigo) represents the strongest FAM fluorescence signal. After incubating the ternary Y-DNA walker with Au@SiO_2@Fe_3O_4 (green), the FAM fluorescence signal of the supernatant was significantly decreased, further confirming the successful coupling of the Y-DNA to the material. Adding Nb.BbvCI to the solution of ternary Y-DNA walker and Au@SiO_2@Fe_3O_4 (black) will drive the ternary Y-DNA walker to cut the track hairpin FAM-cDNA and release FAM signal fragments, and the supernatant after magnetic separation will produce a higher FAM fluorescence signal. The binding of OTA to Apt (red) disrupts the ternary Y-DNA walker and inhibits cleavage. These results demonstrate that the ternary Y-DNA walker can be successfully driven by restriction endonuclease Nb.BbvCI continuously generates a large number of signal fragments, which are inhibited by OTA. After incubating the ternary Y-DNA walker with Au@SiO2@Fe3O4 and Au@Fe3O4 respectively, the FAM fluorescence signal diagram of the supernatant is shown in Fig. 2. The results show that Au@SiO2@Fe3O4 exhibits stronger fluorescence adsorption due to its larger specific surface area.

Moreover, comparing the Au@SiO_2@Fe_3O_4 with Au@Fe_3O_4, the FAM fluorescence signal of the supernatant was compared by incubating the ternary Y-DNA walker with

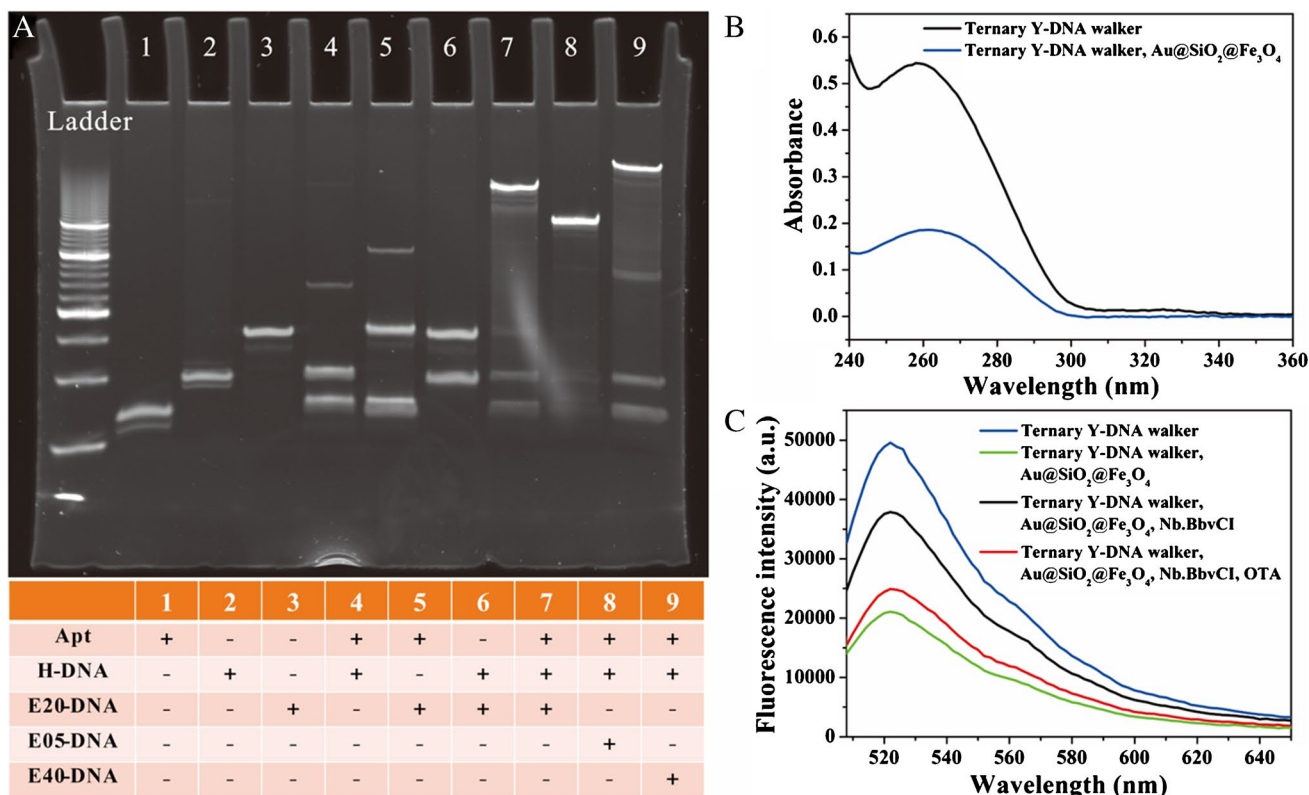|	1	2	3	4	5	6	7	8	9
Apt	+	-	-	+	+	-	+	+	+
H-DNA	-	+	-	+	-	+	+	+	+
E20-DNA	-	-	+	-	+	+	+	-	-
E05-DNA	-	-	-	-	-	-	-	+	-
E40-DNA	-	-	-	-	-	-	-	-	+

Fig. 2 **A** Non- denaturing PAGE (15%) analysis of the Yn-DNA. All samples are run at 200 V for 45 min. The concentration of each sample was set as 400 nM. The down table represents the sample type of each lane; **B** and **C** correspond to UV–vis absorption spectroscopy and fluorescent spectroscopy characterization, respectively

Au@SiO$_2$@Fe$_3$O$_4$ and Au@Fe$_3$O$_4$ respectively. As shown in Fig. S4, Au@SiO$_2$@Fe$_3$O$_4$ exhibits stronger adsorption due to its larger specific surface area.

Optimization of analytical parameters

A series of optimization experiments were conducted on the Au@SiO$_2$@Fe$_3$O$_4$ concentration (Fig. S5A&B), FAM-cDNA volume (Fig. S5C&D), the number of consecutive T bases in Yn-DNA (Constituent En-DNA, $n = 5, 20, 40$) (Fig. S5E&F) and restriction endonuclease Nb.BbvCI cutting time (Fig. S5G&H), 0.5 mg·mL^{-1}, 40 μL, $n = 20$, and 90 min were determined as the optimal experimental conditions, respectively. See Supporting Information (Sect. 2) for more specific optimization procedures.

Analytical performance of ternary Y-DNA walker sensor

Under the optimal experimental conditions, the analytical performance of the ternary Y-DNA walker sensor was evaluated with various concentrations of OTA (100, 50, 10, 5, 1, 0.5, 0.1, 0.05 ng·mL^{-1}). As shown in Fig. 3A, the fluorescence intensity increased gradually as the OTA

concentration decreased from 100 to 0.05 ng·mL^{-1}, and displayed a well-linear relationship with the logarithm of the OTA concentration (Fig. 3B). The regression equation was $F = -3708.85 \lg(c_{OTA}/\text{ng·mL}^{-1}) + 31{,}032.21$ with a good correlation coefficient (R^2) of 0.991, where F is the variable of the FAM fluorescence signal intensity and c is the OTA concentration. Based on the IUPAC [34] method (Sect. 3), the limit of detection (LOD) is estimated to be 0.027 ng·mL^{-1} and Table S2 lists the blank fluorescent signal values when absent of OTA. Compared with other detection methods (Table 1), the ternary Y-DNA walker sensor performed well in terms of linear range and detection limit, indicating that the sensor has good sensing performance.

Specificity and long-term stability

To study the specificity of this strategy, we compared the fluorescence intensity of blank control (Blank), DON, ZEN, AFB$_1$, FB$_1$, OTB, OTA, and a mixture of the above toxins (Mix). Figure 4A and B shows the histogram of fluorescence intensity and Fluorescence spectra of different mycotoxins and their mixture., respectively. In the presence of OTA in the ternary Y-DNA walker sensor, a strong suppression of fluorescence intensity can be observed, confirming the good
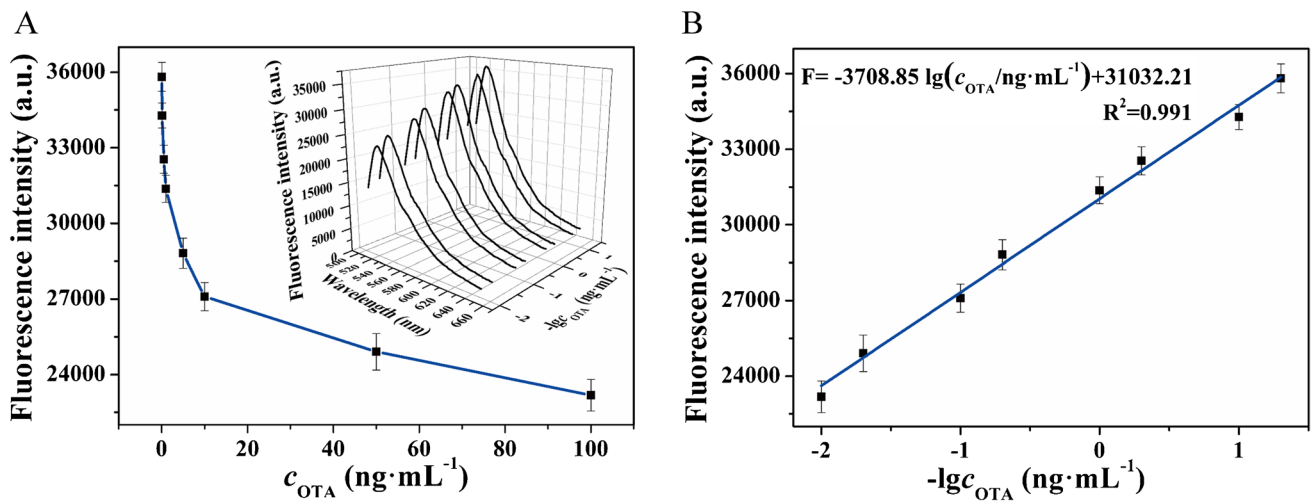
Fig. 3 A Fluorescence intensity of FAM in the supernatant after incubating the ternary Y-DNA walker sensor with different concentrations of OTA and Nb.BbvCI. **B** Calibration curve of FAM fluorescence intensity and -lg[OTA] using ternary Y-DNA walker sensor

Table 1 Comparison of different sensors for the OTA determination

| Method	Linear range	LOD	Ref
Dpy-NhBt-COF@Tb-based fluorescence aptasensor	25–10,000 nM	13.5 nM (5.44 ng·mL^{-1})	[35]
amSWCNTs-based fluorescence aptasensor	1.12–0.08 μM	14 nM (5.64 ng·mL^{-1})	[36]
g-CNQDs and CoOOH nanosheets-based fluorescence aptasensor	57–0.4 ng·mL^{-1}	0.02 ng·mL^{-1}	[37]
Fluorescence aptasensor and RNase H-assisted cycle response strategy	20–0.4 ng·mL^{-1}	0.08 ng·mL^{-1}	[38]
AuNPs-based fluorescence immunosensor and FRET strategy	3.12–0.09 ng·mL^{-1}	0.02 ng·mL^{-1}	[39]
Au@SiO$_2$@Fe$_3$O$_4$-based fluorescence aptasensor and ternary Y-DNA walker strategy	100–0.05 ng·mL^{-1}	0.027 ng·mL^{-1}	This work
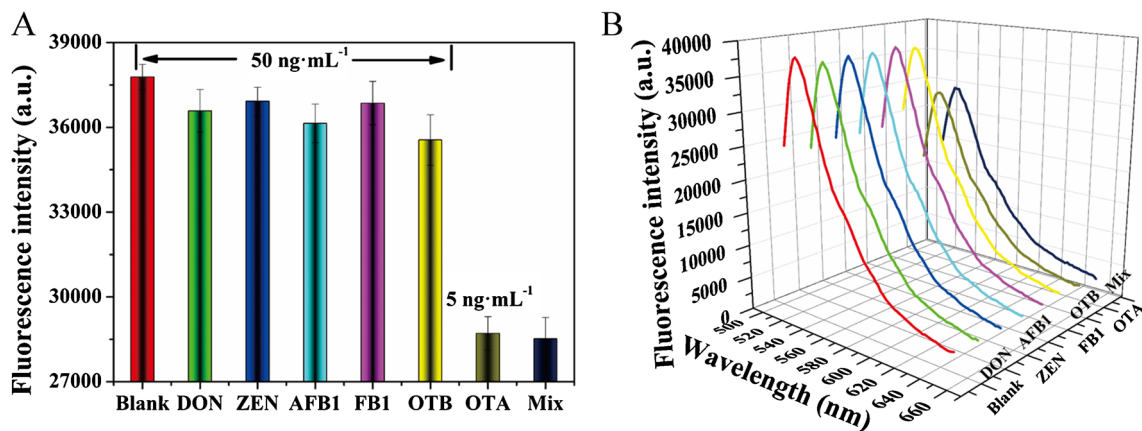
Fig. 4 Histogram of fluorescence intensity (**A**) and fluorescence spectra (**B**) of different mycotoxins and their mixture

specificity of the sensor. The prepared three-way Y-shaped DNA walker sensor was stored in triplicate at 4 °C for 14 days. Then, OTA and Nb.BbvCI were added and fluorescence signals were collected by Synergy H1 Multiplex Detection Microplate Reader. The results showed that the fluorescence intensity was 96.7% of the initial value, which confirmed that the sensing strategy has satisfactory long-term stability.

Ternary Y-DNA walker sensor in real samples

The peanut sample was chosen to investigate the potential application of the ternary Y-DNA walker sensor. According to the toxicological assessment conducted by the Food Science Committee [40] and IARC's [3] assessment of the carcinogenic risk of chemicals to humans, the maximum allowable content of OTA in cereals is 5 ng·mL^{-1}, and in cereal-derived products is 3 ng·mL^{-1}. The OTA spiked concentrations used in the study were 0.5, 1, 5, 10, and 50 ng·mL^{-1}, respectively. These specimens were measured by the developed method and a commercially available ELISA method. As shown in Fig. S6, the results show that there is no significant difference between the two methods and that they are highly correlated. As shown in Table S3, the results showed that recovery rates in the peanut sample was 82.00–93.30% with relative standard deviations (RSD) of 3.36–5.14%. These experimental results showed that the fluorescence aptasensor based on the ternary Y-DNA walker strategy could be used for the detection of real samples and had broad application prospects in identifying OTA and realizing control of it in food safety as well.

Conclusions

Overall, based on the Au@SiO$_2$@Fe$_3$O$_4$ nanomaterials and ternary Y-DNA walker amplification strategy, a fluorescence aptasensor was developed for OTA detection. As a loading platform for fluorescent sensors, Au@SiO$_2$@Fe$_3$O$_4$ nanomaterials can greatly improve the distribution density of the ternary Y-DNA walker, and can be easily recovered and magnetically separated. The ternary Y-DNA walker couples the nanomaterials via Au–S covalent bonds, resulting in satisfactory stability of the sensor. Moreover, the ternary Y-DNA walker was programmed to cleave the FAM probe driven by the restriction endonuclease Nb.BbvCI, and this driving process was inhibited by OTA. Taking advantage of the aforementioned advantages, the proposed sensing strategy exhibits satisfactory analytical performance. It is worth noting that both the design of Au@SiO$_2$@Fe$_3$O$_4$ nanomaterials and ternary Y-DNA walker can be used to develop biosensors for other targets. In this study, Yn-DNA was optimized in more detail, so that it can easily expand to other targets by replacing different aptamers in the base sequence of the Yn-DNA binding region. The current detection strategy relies on a multi-step standardized incubation process, which limits the scale and frequency of monitoring required. In the future, investing in high-throughput detection equipment may improve this situation.

Abbreviations OTA: Ochratoxin A; CONTAM: Contaminants in the Food Chain; BMDL$_{10}$: Benchmark dose limit; ssDNA: Single-stranded DNA; Au@SiO$_2$@Fe$_3$O$_4$: Iron oxide and silica core–shell loaded gold nanoparticles composites; FAM: Carboxyfluorescein; Apt: Aptamer; ZEN: Zearalenone; DON: Deoxynivalenol; AFB$_1$: Aflatoxin B$_1$; FB$_1$: Fumonisin B$_1$; PAA: Poly (acrylic acid); Tris-base: Tris(hydroxymethyl)aminomethane; TEOS: Tetraethyl orthosilicate; TCEP: Tris(hydroxymethyl) aminomethane phosphine hydrochloride solution; PEI: Polyethylenimine; TEM: Transmission electron microscope; SEM: Scanning electron microscopy; XRD: X-ray diffractometer; RSD: Relative standard deviations

Declarations

Conflict of interest The authors declare no competing interests.

References

1. Dey DK, Kang JI, Bajpai VK, Kim K, Lee H, Sonwal S, Simal-Gandara J, Xiao J, Ali S, Huh YS, Han YK, Shukla S (2022) Mycotoxins in food and feed: toxicity, preventive challenges, and advanced detection techniques for associated diseases. Crit Rev Food Sci Nutr:1–22. https://doi.org/10.1080/10408398.2022.2059650

2. Shotwell OL, Hesseltine CW, Goulden ML (1969) Ochratoxin A: occurrence as natural contaminant of a corn sample. Appl Microbiol 17(5):765–766. https://doi.org/10.1128/am.17.5.765-766.1969

3. IARC (1993) Some naturally occurring substances: food items and constituents, heterocyclic aromatic amines and mycotoxins. In: IARC Monographs on the Evaluation of Carcinogenic Risk of Chemicals to Humans No 56, which met in Lyon, 9–16 June 1992. International Agency for Research on Cancer, Lyon (FR). http://monographs.iarc.fr/ENG/Monographs/vol56/mono56.pdf

4. Al-Dhahebi AM, Jose R, Mustapha M, Saheed MSM (2022) Ultrasensitive aptasensor using electrospun MXene/polyvinylidene fluoride nanofiber composite for Ochratoxin A detection. Food Chem 390:133105. https://doi.org/10.1016/j.foodchem.2022.133105

5. Schrenk D, Bodin L, Chipman JK, del Mazo J, Grasl-Kraupp B, Hogstrand C, Hoogenboom L, Leblanc JC, Nebbia CS, Nielsen E, Ntzani E, Petersen A, Sand S, Schwerdtle T, Vleminckx C, Wallace H, Alexander J, Dall'Asta C, Mally A, Metzler M, Binaglia M, Horvath Z, Steinkellner H, Bignami M, Chain EPCF (2020) Risk assessment of ochratoxin A in food. EFSA J 18(5):6113. https://doi.org/10.2903/j.efsa.2020.6113

6. Kochman J, Jakubczyk K, Janda K (2021) Mycotoxins in red wine: Occurrence and risk assessment. Food Control 129:108229. https://doi.org/10.1016/j.foodcont.2021.108229

7. Meira DI, Barbosa AI, Borges J, Reis RL, Correlo VM, Vaz F (2023) Recent advances in nanomaterial-based optical biosensors for food safety applications: Ochratoxin-A detection, as case study. Crit Rev Food Sci Nutr:1–43. https://doi.org/10.1080/10408398.2023.2168248

8. Mirsadoughi E, Pebdeni AB, Hosseini M (2023) Sensitive colorimetric aptasensor based on peroxidase-like activity of ZrPr-MOF to detect Salmonella Typhimurium in water and milk. Food Control 146:109500. https://doi.org/10.1016/j.foodcont.2022.109500

9. Hong C, Wang J, Wang Y, Huang Z, Yang H, Yang D, Cai R, Tan W (2022) Fluorescence detection of milk allergen beta-lactoglobulin based on aptamers and WS(2) nanosheets. J Mater Chem B 10(35):6752–6757. https://doi.org/10.1039/d2tb00263a

10. Steinmetzger C, Bauerlein C, Hobartner C (2020) Supramolecular fluorescence resonance energy transfer in nucleobase-modified fluorogenic RNA aptamers. Angew Chem Int Ed Engl 59(17):6760–6764. https://doi.org/10.1002/anie.201916707

11. Huang K, Chen X, Li C, Song Q, Li H, Zhu L, Yang Y, Ren A (2021) Structure-based investigation of fluorogenic Pepper aptamer. Nat Chem Biol 17(12):1289–1295. https://doi.org/10.1038/s41589-021-00884-6

12. Khosropour H, Kalambate PK, Kalambate RP, Permpoka K, Zhou X, Chen GY, Laiwattanapaisal W (2022) A comprehensive review on electrochemical and optical aptasensors for organophosphorus pesticides. Mikrochim Acta 189(9):362. https://doi.org/10.1007/s00604-022-05399-y

13. Dong X, Qi S, Qin M, Sun Y, Lv Y, Zhang Y, Wang Z (2023) A novel biomimetic network amplification strategy designed fluorescent aptasensor based on yolk-shell Fe(3)O(4) nanomaterials for aflatoxin B1 detection. Food Chem 398:133761. https://doi.org/10.1016/j.foodchem.2022.133761

14. Sun Y, Zhao J, Liang L (2021) Recent development of antibiotic detection in food and environment: the combination of sensors and nanomaterials. Mikrochim Acta 188(1):21. https://doi.org/10.1007/s00604-020-04671-3

15. Mahani M, Faghihi-Fard M, Divsar F, Torkzadeh-Mahani M, Khakbaz F (2022) Ultrasensitive FRET-based aptasensor for interleukin-6 as a biomarker for COVID-19 progression using nitrogen-doped carbon quantum dots and gold nanoparticles. Mikrochim Acta 189(12):472. https://doi.org/10.1007/s00604-022-05570-5

16. Shi X, Zhu X, Chai Y, Zhou Y, Yuan R (2023) Non-enzymatic electrochemiluminescence biosensor for ultrasensitive detection of ochratoxin A based on efficient DNA walker. Food Chem 407:135113. https://doi.org/10.1016/j.foodchem.2022.135113

17. Qiao X, Ma X, Ma X, Yue T, Sheng Q (2021) A label-free aptasensor for ochratoxin a detection with signal amplification strategies on ultrathin micron-sized 2D MOF sheets. Sensors Actuators B: Chem 334. https://doi.org/10.1016/j.snb.2021.129682

18. Wu R, Guo J, Wang M, Liu H, Ding L, Yang R, Liu LE, Liu Z (2023) Fluorescent sensor based on magnetic separation and strand displacement amplification for the sensitive detection of Ochratoxin A. ACS Omega 8(17):15741–15750. https://doi.org/10.1021/acsomega.3c01408

19. Wang Y, Song W, Zhao H, Ma X, Yang S, Qiao X, Sheng Q, Yue T (2021) DNA walker-assisted aptasensor for highly sensitive determination of Ochratoxin A. Biosens Bioelectron 182:113171. https://doi.org/10.1016/j.bios.2021.113171

20. Chandrasekaran AR, Anderson N, Kizer M, Halvorsen K, Wang X (2016) Beyond the fold: Emerging biological applications of DNA origami. ChemBioChem 17(12):1081–1089. https://doi.org/10.1002/cbic.201600038

21. Sundaresan SM, Fothergill SM, Tabish TA, Ryan M, Xie F (2021) Aptamer biosensing based on metal enhanced fluorescence platform: A promising diagnostic tool. Appl Phys Rev 8(4):041311. https://doi.org/10.1063/5.0065833

22. Qi S, Dong X, Sun Y, Zhang Y, Duan N, Wang Z (2022) Split aptamer remodeling-initiated target-self-service 3D-DNA walker for ultrasensitive detection of 17beta-estradiol. J Hazard Mater 439:129590. https://doi.org/10.1016/j.jhazmat.2022.129590

23. Taghdisi SM, Danesh NM, Ramezani M, Emrani AS, Abnous K (2018) Novel colorimetric aptasensor for zearalenone detection based on nontarget-induced aptamer walker, gold nanoparticles, and exonuclease-assisted recycling amplification. ACS Appl Mater Interfaces 10(15):12504–12509. https://doi.org/10.1021/acsami.8b02349

24. Ji Y, Zhang L, Zhu L, Lei J, Wu J, Ju H (2017) Binding-induced DNA walker for signal amplification in highly selective electrochemical detection of protein. Biosens Bioelectron 96:201–205. https://doi.org/10.1016/j.bios.2017.05.008

25. Ullah S, Zahra QUA, Mansoorianfar M, Hussain Z, Ullah I, Li W, Kamya E, Mehmood S, Pei R, Wang J (2022) Heavy Metal Ions Detection Using Nanomaterials-Based Aptasensors. Crit Rev Anal Chem 1–17. https://doi.org/10.1080/10408347.2022.2115287

26. Dong Q, Jia X, Wang Y, Wang H, Liu Q, Li D, Wang J, Wang E (2022) Sensitive and selective detection of Mucin1 in pancreatic cancer using hybridization chain reaction with the assistance of Fe(3)O(4)@polydopamine nanocomposites. J Nanobiotechnology 20(1):94. https://doi.org/10.1186/s12951-022-01289-w

27. Wang C, Qian J, Wang K, Hua M, Liu Q, Hao N, You T, Huang X (2015) Nitrogen-Doped Graphene Quantum Dots@SiO2 nanoparticles as electrochemiluminescence and fluorescence signal indicators for magnetically controlled aptasensor with dual detection channels. ACS Appl Mater Interfaces 7(48):26865–26873. https://doi.org/10.1021/acsami.5b09300

28. Alterary SS, AlKhamees A (2021) Synthesis, surface modification, and characterization of Fe3O4@SiO2 core@shell nanostructure. Green Processing Synthesis 10(1):384–391. https://doi.org/10.1515/gps-2021-0031

29. Rakhtshah J (2022) A comprehensive review on the synthesis, characterization, and catalytic application of transition-metal Schiff-base complexes immobilized on magnetic Fe3O4 nanoparticles. Coord Chem Rev 467:214614. https://doi.org/10.1016/j.ccr.2022.214614

30. Cruz-Aguado JA, Penner G (2008) Determination of ochratoxin a with a DNA aptamer. J Agric Food Chem 56(22):10456–10461. https://doi.org/10.1021/jf801957h

31. Xu G, Zhao J, Liu N, Yang M, Zhao Q, Li C, Liu M (2019) Structure-guided post-SELEX optimization of an ochratoxin A aptamer. Nucleic Acids Res 47(11):5963–5972. https://doi.org/10.1093/nar/gkz336

32. Song ZW, Zhu JM, Jiang LY (2014) Novel polysiloxaneimide/polyetherimide/non-woven fabric composite membranes for organophilic pervaporation. J Membr Sci 472:77–90. https://doi.org/10.1016/j.memsci.2014.08.040

33. Manshad S, Isloor AM, Nawawi MGM, Inamuddin KI, Marwani HM (2020) Pervaporation dehydration of bio-fuel (n-butanol) by dry thermal treatment membrane. Mater Res Express 7(6):065001. https://doi.org/10.1088/2053-1591/ab9562

34. Shrivastava A, Gupta V (2011) Methods for the determination of limit of detection and limit of quantitation of the analytical methods. Chronicles Young Scientists 2(1):21. https://doi.org/10.4103/2229-5186.79345

35. Yu Y, Li G (2022) Design of terbium (III)-functionalized covalent organic framework as a selective and sensitive turn-on fluorescent switch for ochratoxin A monitoring. J Hazard Mater 422:126927. https://doi.org/10.1016/j.jhazmat.2021.126927

36. Ranganathan V, Boisjoli S, DeRosa MC (2022) Adsorption-desorption nano-aptasensors: fluorescent screening assays for ochratoxin A. Rsc Adv 12(22):13727–13739. https://doi.org/10.1039/d2ra00026a

37. Bi X, Luo L, Li L, Liu X, Chen B, You T (2020) A FRET-based aptasensor for ochratoxin A detection using graphitic carbon nitride quantum dots and CoOOH nanosheets as donor-acceptor pair. Talanta 218:121159. https://doi.org/10.1016/j.talanta.2020.121159

38. Wu K, Ma C, Zhao H, Chen M, Deng Z (2019) Sensitive aptamer-based fluorescene assay for ochratoxin A based on RNase H signal amplification. Food Chem 277:273–278. https://doi.org/10.1016/j.foodchem.2018.10.130

39. Serebrennikova KV, Samokhvalov AV, Zherdev AV, Dzantiev BB (2022) A fluorescence immunosensor for ochratoxin A based on resonance energy transfer between fluorescein derivative and gold nanoparticles. J Food Compos Anal 114:104806. https://doi.org/10.1016/j.jfca.2022.104806

40. Commission E (2012) Commission Regulation (EU) No. 594/2012 amending Regulation (EC) 1881/2006 as regards the maximum levels of the contaminants ochratoxin A, non dioxin-like PCBs and melamine in foodstuffs. Off J Eur Union 43:43–45